Supplementary Information

Tough hydrogel with high water content and ordered fibrous structures as artificial human ligament

Songjiu Han,[a, b] Qirui Wu,[a, b] Jundong Zhu,[a] Jiayu Zhang,[a] Anbang Chen,[a] Shu Su,[c] Jiantao Liu,[b] Jianren Huang,*[a] Xiaoxiang Yang,[b] Lunhui Guan,*[a]

a. CAS Key Laboratory of Design and Assembly of Functional Nanostructures, Fujian Key Laboratory of Nanomaterials, Fujian Institute of Research on the Structure of Matter, Chinese Academy of Sciences, Fuzhou 350108, China.

b. School of Mechanical Engineering and Automation, Fuzhou University, Fuzhou 350108, China

c. Fujian College Association Instrumental Analysis Center, Fuzhou University, Fuzhou, Fujian, 350108, China

KEYWORDS. Tough hydrogel, Fracture resistance, Artificial ligament

Experimental Section

Preparation of the unidirectional freeze-casted of PVA@CNT hydrogels.

Firstly, 10 wt. % PVA aqueous solution was prepared by dissolving the PVA powers in deionized water at 90 ºC for 4 hours. and 1 wt.% CNT aqueous solution was prepared by dispersing the CNT powers in deionized water, the dispersant was contented at 25% of the CNT mass. After complete degassing, the PVA@CNT aqueous solution was transferred into the Teflon mold, which was placed on the top of a copper billet, and half of the copper billet was submerged in liquid nitrogen. The icicles grow upward along the temperature gradient created by the copper block. Once the freeze-casting process was completed, the samples were placed in a freeze dryer at -80 ºC and 1 Pa pressure for 36 hours. The obtained dry aerogel samples were annealed under a compression pressure of 100 kPa at 100 ºC for 90 minutes, followed by soaking in a sodium citrate salt solution for 24 hours, and finally, the obtained anisotropic tough hydrogels were soaked in deionized water 24 hours to remove excess salt ions.

Preparation of the Freeze-thawed PVA@CNT hydrogels. To obtain freeze-thawed hydrogels with random structures, the PVA@CNT solution was degassed and transferred into molds, then frozen at -20 ºC for 8 hours, following by thawing at room temperature for 3 hours. The freeze-thawed process was repeated 5 times to obtain FT PVA@CNT hydrogels.

Characterization of PVA@CNT hydrogels.

For probing the anisotropic microstructures of the PVA@CNT hydrogels, the morphology observation was conducted was conducted on a Field-emission Scanning Electron Microscopy. All hydrogel samples were freeze-dried in advance, then fractured in liquid nitrogen. The fracture surfaces the sprayed with gold using an ion-sputtering device, and then observed for microstructure. The chemical structure of prepared gel samples was analyzed by X-ray diffraction (XRD), differential scanning calorimetry (DSC), and Raman spectra. Raman spectra were performed on a Dilor LABRAM-1B multi-channel confocal microspectrometer with a 532 nm laser excitation. XRD analyses were performed on an X-ray diffractometer (DY5261/Xpert3,

CEM, America) with the Cu K α radiation (40 kV, 40 mA, λ = 1.542 nm) at 2θ of ranging from 5 to 85°. The DSC scans were carried out a differential scanning calorimeter instruments (DSC214, Netzsch, GER) in a nitrogen atmosphere at a range of −120 °C with a heating rate of 10 °C min^{-1}.

Measurement of water content.

All hydrogel samples were soaked into deionized water until equilibrium, the corresponding weight is the equilibrium-swollen ($m_{swollen}$). Then, these hydrogel samples were placed in air at 35 ºC for 12 hours and finally in a drying oven at 90 ºC for 4 hours until the moisture was completely removed, and the weight is the fully-dried state (X_{dry}). The water content (θ_{water}) of the fully-swollen samples were calculated as $\theta water = \left(m_{swollen} - m_{dry}\right) \Big/ m_{swollen} \times 100\%$.[10]

Measurement of the crystallinity in swollen samples.

We measured the crystallinities of all PVA@CNT hydrogels by differential scanning calorimetry (DSC, TA), following the previously-reported protocol.[11] All the samples were first chemically crosslinked with excessively glutaraldehyde to fix the amorphous phase, then dried the samples at 37 ºC for 2 hours. We weighted the total mass of the air-dried sample (m_{total}), the mass of the residual water ($m_{residual}$) and the mass of crystalline domains ($m_{crystalline}$) in a Tzero pan and heated up from 50 to 250 ºC at the rate of 20 ºC min^{-1} under a nitrogen atmosphere with a flow rate of 30 mL/min. A broad peak was observed in the temperature range from 60 to 160 ºC, which corresponding to the evaporation of residual water molecules. The enthalpy for water evaporation per mass unit of dried sample (with residual water) $H_{residual}$ was calculated by integrating the endothermic peak in the temperature range of 60 to 160 ºC. the formula for the mass of the residual water is $m_{residual} = m_{total} \times \left(H_{residual} \Big/ H^{0}_{water}\right)$, where $H^{0}_{water} = 2260 \text{ J g}^{-1}$ is the latent heat for water evaporation. The other narrow peak ranging from 200 to 250 ºC corresponding to the melting temperature of the crystalline domains. The enthalpy

for melting the crystalline domains per mass unit of the dry sample (with residual water) $H_{residual}$ can be estimated by integrating the endothermic transition ranging from 200 to 250 °C. Thus, the mass of the crystalline domains $m_{residual}$ can be calculated as $m_{crystalline} = m_{total} \times \left(H_{crystalline} / H^{0}_{crystalline} \right)$, where $H^{0}_{crystalline} = 138.6\,\mathrm{J\ g^{-1}}$ is the enthalpy of melting of 100% crystalline PVA. Therefore, the crystallinity of dry samples X_{dry} (without residual water) can be calculated as $X_{dry} = m_{crystalline} / \left(m_{total} - m_{residual} \right) \times 100\%$. With measured water content, the crystallinity in the swollen state can be calculated as $X_{swollen} = X_{dry} \times \left(1 - \theta_{water} \right)$.

Tensile test and Fatigue threshold of the hydrogel samples.

We tested all tensile experiments with an electronic universal testing machine (AG-X plus, SHIMADZU, Japan), which equipped with a maximum force of 500-N loading cell. All fully swollen samples (6 cm (*L*) × 7 mm (*W*) × 2 mm (*t*)) were in strip form and stretched at room temperature. All experimentals were performed using the same stretch speed of 50 mm s^{-1}. The normal stress, S, was calculated as $F / \left(w \times t \right)$, where F are the recorded force. The stretch, λ , was calculated as $\lambda = L_C / L_0 + 1$, where L_C and L_0 are measuring distance and initial distance between the two grippers, respectively.

The single-notch method was used to quantify the fatigue threshold of the hydrogel samples, and all cyclic tensile tests were performed on fully swollen samples, using a flexible electronic tester in a water bath to avoid dehydration-induced crack propagation during prolonged stretching. Pre-cracked samples were cyclically stretched at different maximum stretches λ_{MAX} , and the crack propagated cycle by cycle was recorded by a high-speed camera. To represent fatigue fracture of a material, it is common to plot the extension of crack per cycle, d_C / d_N , as a function of the rate of energy release. Following previous studies of fatigue fracture of hydrogels, we integrated the stress-

stretch curve of the samples without cutting notch to calculate the energy density $W(\lambda_{MAX})$. The effective energy release rate is $G = HW(\lambda_{MAX})$.[1]**Finite-Element analysis simulation.**

In the finite-element analysis simulation (Figure 3e, 3f), Corresponding to the related SEM image, the ABAQUS secondary development interfaces were conducted to construct the random fibers and a matrix model. Python language was used to establish a long fiber model with parallel orientation distribution: fully oriented and randomly distributed. Uniaxial tensile boundary conditions were applied for elastic deformation simulation, and the experimental uniaxial tensile elastic modulus E and Poisson's ratio v were brought in. The numerical results are in good agreement with the experimental results. At the same time, the embedded element technology is applied, and the matrix is set as the host element and the fiber is set as the embedded element. The mesh quality is improved by setting the margin between the Host element and the embedded element. Then, the fibers were embedded in the matrix for simulated tensile tests. Since the modulus of the fibers is much higher than that of the matrix, the stress distribution on the fiber will be more obvious under the same tension as well as demonstrated in the stress gradient nephogram. The FT hydrogel is considered to equal with the matrix materials with CNTs, and FC and FCAS hydrogel are embedded with fibers of different strengths in the matrix.

Establishment of representative volume element at the microscopic scale

In order to accurately characterize the mechanical behavior of a macroscale object, it is desirable to take into account the microscopic properties of matter in the modeling. Generally, the representative volume element (RVE) is used to construct micro-scale structure and performance[13].The python scripting language was used to generate randomly distributed CNT fibers in the model. Using the RSA algorithm, fibers were generated continuously in the model. The fiber orientation in the model is completely random, and the orientation Angle is a random number between $(\pi/-2, \pi/2)$. In the RVE model, carbon nanotubes are introducing into the PVA matrix. This phenomenon is similar to concrete structures where other fillers are incorporated into the cement to

form a filler network. The modulus of the fillers is generally higher than that of the matrix, hence the presence of this rigid network will increase the strength of the overall materials.

Knee joint bionic Test and Biocompatibility Test.

To verify the possibility and reliability of our hydrogel material as an artificial ligament, we immobilized our tough hydrogel on an artificially fabricated knee joint model, and using a soft wire rope to pull the leg bone model for flexion, in which the dynamic part used a flexible electronic tester to reciprocate. In order to prevent the evaporation of moisture during long-term bending experiments, the whole model was placed in a transparent box made of acrylic sheet and is equipped with an aerosol humidifier to simulate the humid environment of the human body. At the same time, a digital source meter was used to collect the resistance change during the stretching process to monitor the working state of our artificial ligament. The CCK8 assay was used to assess the effect of materials on the vitro cytotoxicity of Human umbilical vein endothelial cells (HUVECs). The material was first sterilized by UV light to ensure that the specimen remained sterile. The resuscitated HUVECs were then counted and the concentration of the cell suspension concentration was adjusted by the addition of medium. Where after, the cells were seeded on 96-well plates (1×104 cells/well) and incubated for at 37 ^{o}C with 5% CO_2 atmosphere for 24 h in incubator. Therewith, the materials were co-cultured with the cells for 24 h, 72 h and 120 h, respectively. Subsequently, HUVECs were washed with phosphate buffer saline (PBS), and 20 μL of CCK-8(MCE, America) solution was instilled to each well. Then after that, the liquid was inhaled into a 96-well plate, and the absorbance at 450 nm was measured with an enzyme marker (EPOCH2, Biotek). The group containing cells, medium, CCK-8 and without material were used as the control group, and the cell viability of the control group was set at 100%. The cell relative viability was calculated from the obtained optical density (OD) values. Therefore, the cell relative viability of HUVECs in the experimental group = OD experimental group/OD control group×100%. Finally, Finally, the morphology of cells stained with Calcein-AM (BestBio, Shanghai) reagent was observed by fluorescence microscope (DMI8, Leica).

Electrical Output Measurement:

The current signal of the sensing unit generated by artificial ligament and sensor was acquired by a digital source meter (Keithley 2450). The samples are match to the strain changes of different body joints, and the body movement were collected with electrical signal acquisition (DAQ,TruEbox-01RC) for sampling.

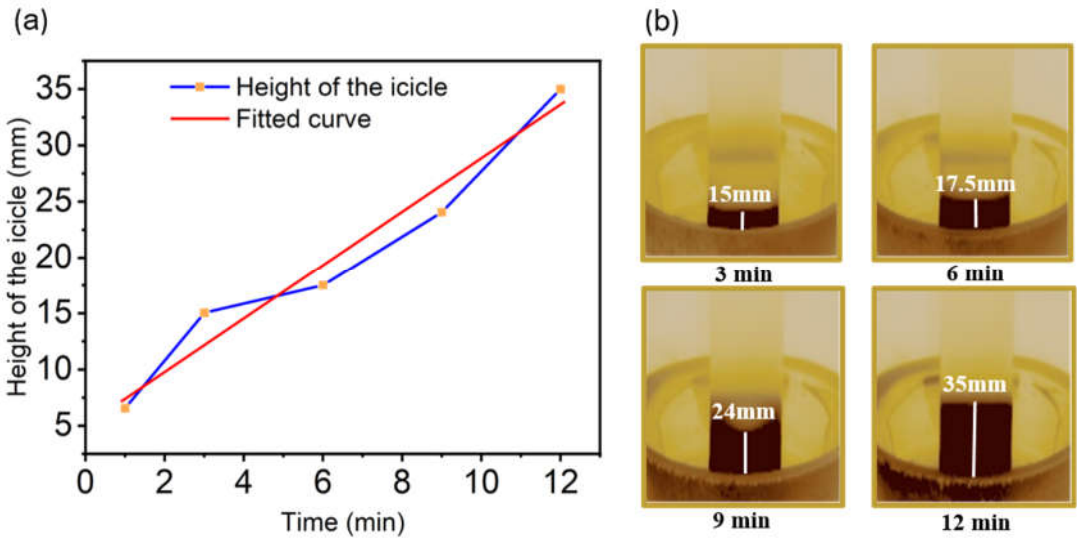

Figure S1. Infrared thermal images and icicle growth curves.

The long-range and ordered degree of fibers is related to the growth rate of icicles. The degree of fibrosis was higher when the rate of icicle growth was more constant. The temperature gradient is directly related to the growth rate of the icicle. Therefore, we controlled the temperature through infrared monitoring to obtain relatively uniform fibers (Figure S1).

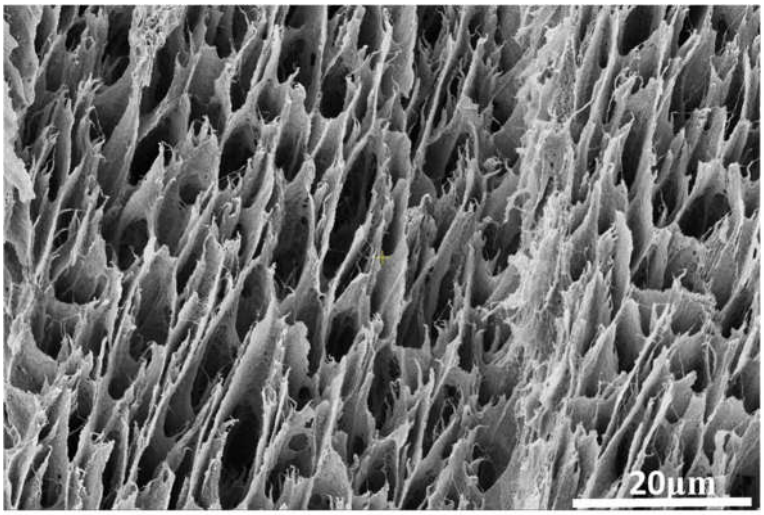

Figure S2. The SEM image of the cross-section view of the oriented structure presents honeycomb-like holes and the CNTs network.

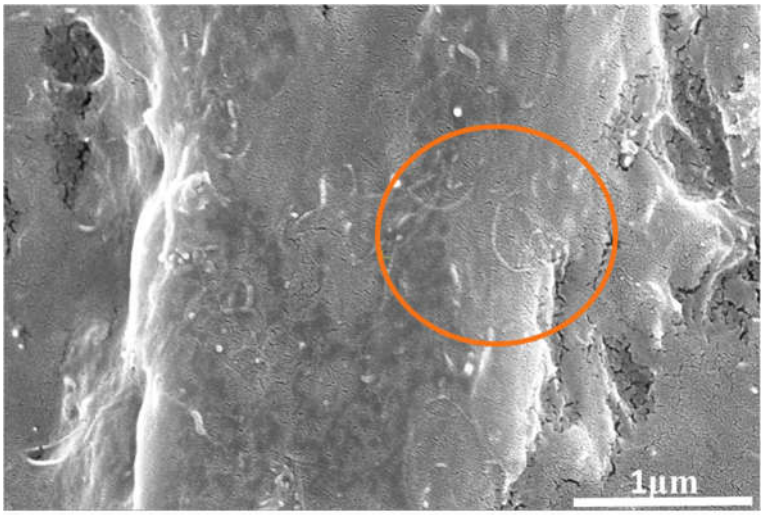

Figure S3. The SEM image of CNTs network.

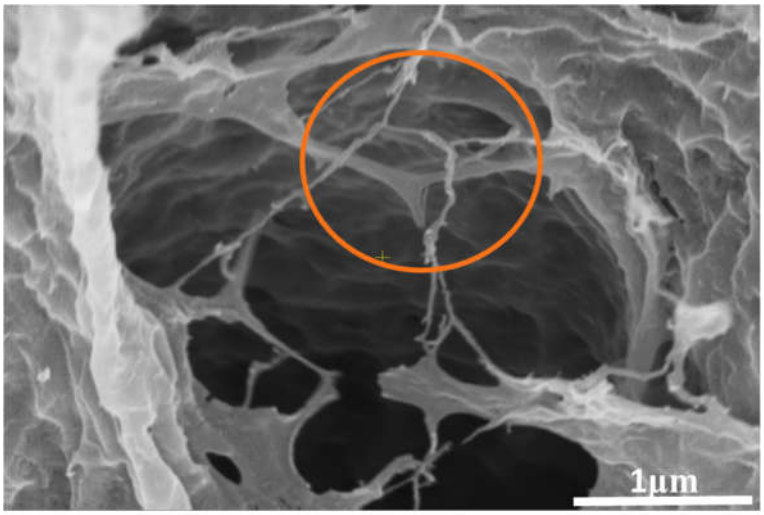

Figure S4. The SEM image of bridge in theCNTs network.

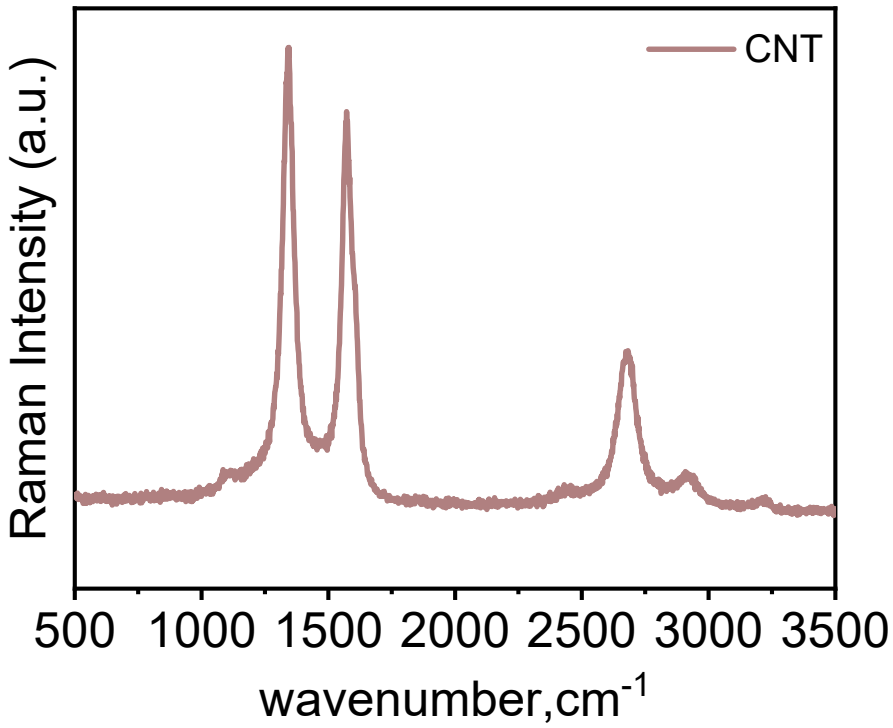

Figure S5. Raman spectra of CNTs in the wavenumber ranges from 500 to 3500 cm^{-1}

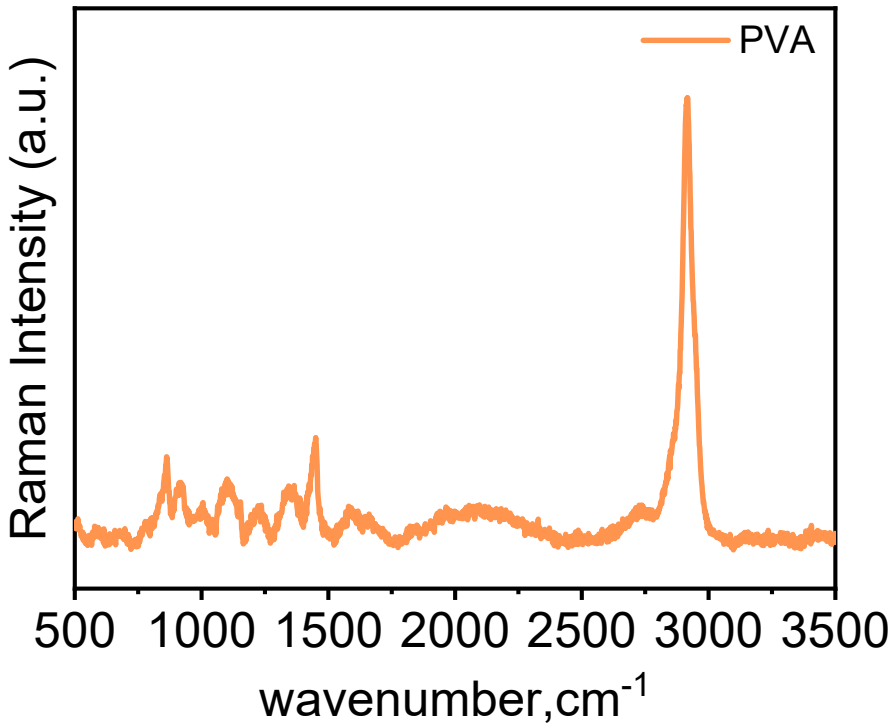

Figure S6. Raman spectra of PVA in the wavenumber ranges from 500 to 3500 cm^{-1}

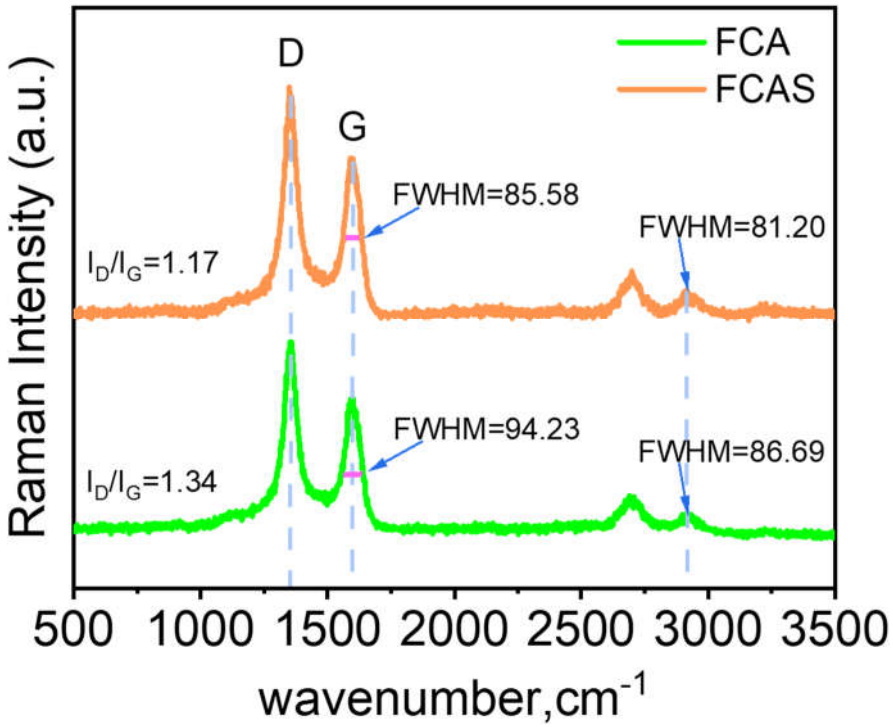

Figure S7. Raman spectra of FCA and FCAS hydrogels. in the wavenumber ranges from 500 to 3500 cm^{-1}

In the Raman spectroscopy (Figure S5), which shows three characteristic peaks for pure CNT9 (D band at 1344.78 cm^{-1} and G band at 1572.02 cm^{-1}). In Figure S6, the Raman peak of pure PVA at 2916.71 cm^{-1}. Compared with the G-band of pure CNT (1572.02 cm^{-1}), a slight up-shift of the G band has been observed with FCA and FCAS. (1952.08 cm^{-1} and 1596.71 cm^{-1}, Figure S7). This up-shift indicates significant unbundling of the CNT. Which means that the CNTS are more uniformly dispersed in the PVA matrix. Moreover, the I_G/I_D value of FCAS is 0.85, which is higher than that of FCA of 0.74. It can be explained that the degree of ordering of CNTs is higher as the ordering of the PVA matrix nano-crystallites increases after salting out. Meanwhile, the comparison of the Full Width at Half Maxima (FWHM) of FCAS and FCA (85.58 and 94.23, respectively) further illustrate the orderly strengthening of the FCAS network.

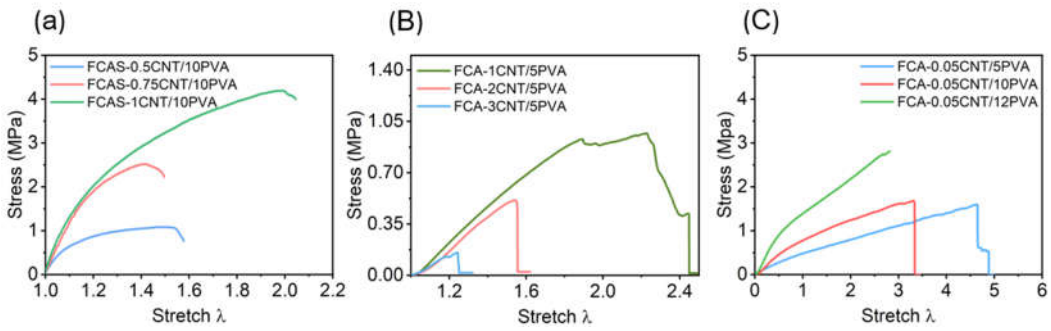

Figure S8. The tensile stress-stretch curves corresponding to different CNTs content and PVA weight.

In supplementary Figure S8a, in the case of light mass fraction, the tensile strength of the hydrogel sample is significantly improved with the increase of CNT content; in supplementary Figure S8b, under the premise of large mass fraction, with the increase of CNTs, the maximum stress and the stretch amount both decreased. Consequently, the mainly content of the samples was determined to be 1 wt%. In addition to exploring the effect of CNTs content on mechanical properties of the hydrogels, we also explored the effect of PVA concentration (Figure S8c). We changed the initial PVA concentration of 5 wt.%, 10 wt.% and 12 wt.%, and reached ultimate stresses of 1.6 MPa, 2.0 MPa and 2.8 MPa and related maximum stretch of 4.9, 4.45 and 3.8. By comparing the tensile tests of samples with different PVA mass fractions, it is found that the mass of PVA was directly proportional to the tensile strength of the final hydrogel sample, and on the contrary, it was inversely proportional to the amount of stretching. However, considering the influence of CNTs' network occupying some volume on the overall sample. And combined with the actual test, it is difficult to melt PVA when the content of PVA is greater than 10%. Consequently, based on this analysis, which including the tensile test and the difficulty of melting PVA, the final content of PVA is determined to be 10 wt.%.

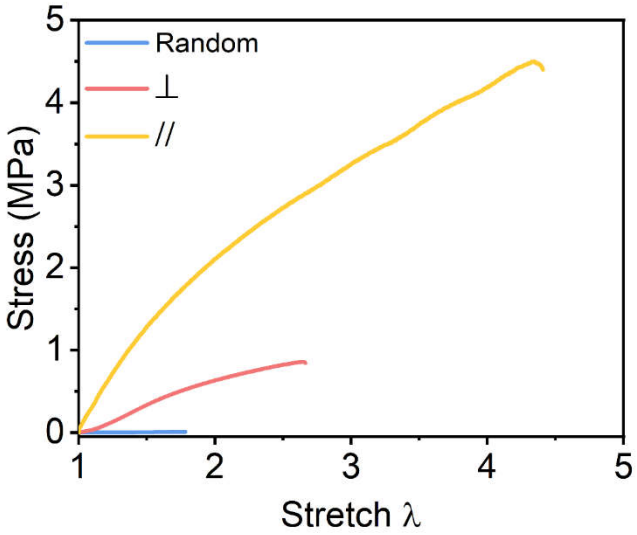

Figure S9. Tensile curves for different fiber orientations.

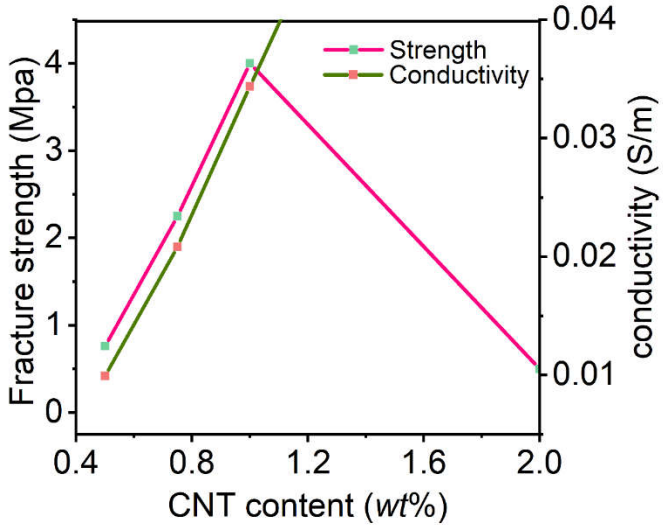

Figure S10. The synergistic impact of conductivity and the tensile strength of the FCAS with different CNTs concentrations.

As shown in Figure S10, the increase of CNTs content caused the conductivity of the hydrogel to rise rapidly, but the corresponding mechanical properties displayed fluctuations. Excessive CNTs loading resulted in the decline of mechanical properties of FCAS. It is explained as over a certain amount of filler network hindered the crosslinking of the matrix network. Due to the agglomerate and in homogeneity of the overall material, causing the mechanical properties were deteriorated.

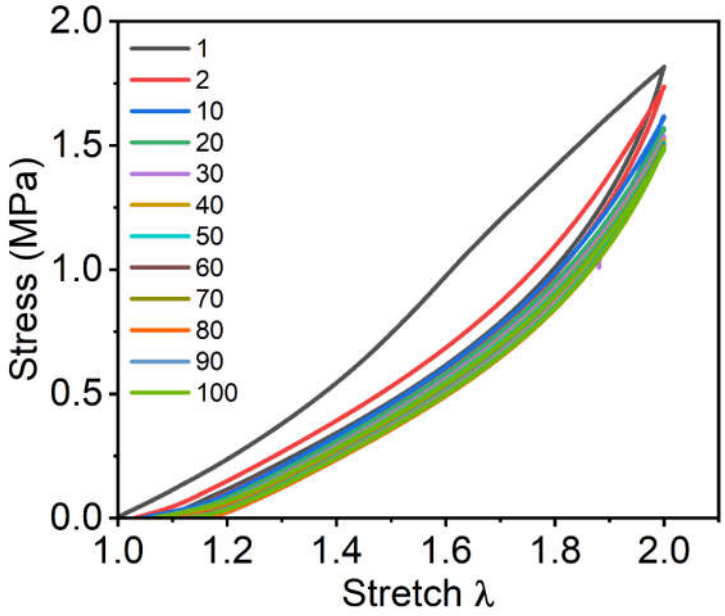

Figure S11. The repeatability and reversibility of the FCAS hydrogels.

In Figure S11, after the first cycle of loading-unloading stretching, the subsequent loading-unloading curves basically coincide. The hysteresis area did not obvious increase over 100 cycles, which suggested that the sacrificial hydrogen bonds were almost recoverable. And most of the irrecoverable bond energy was consumed in the first lap, demonstrating the fatigue resistance performance.

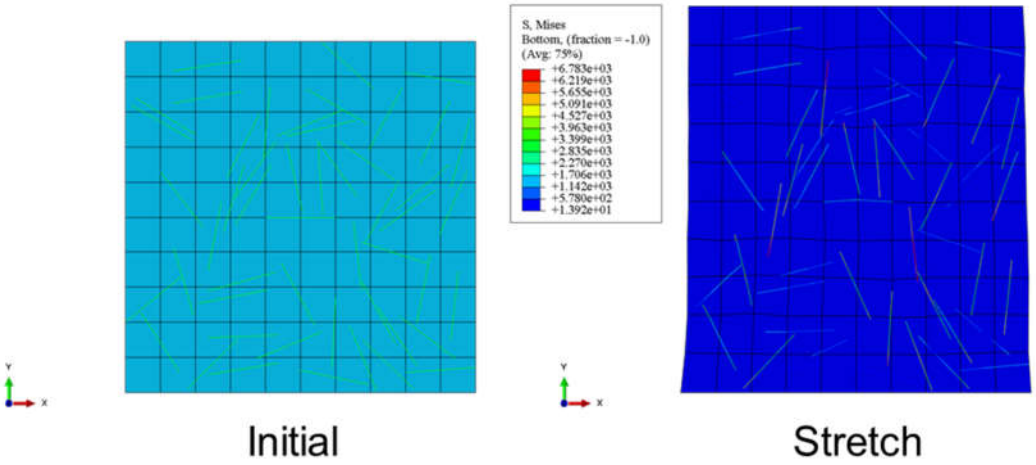

Figure S12. The simulation of the RVE model of the PVA@CNT hydrogels.

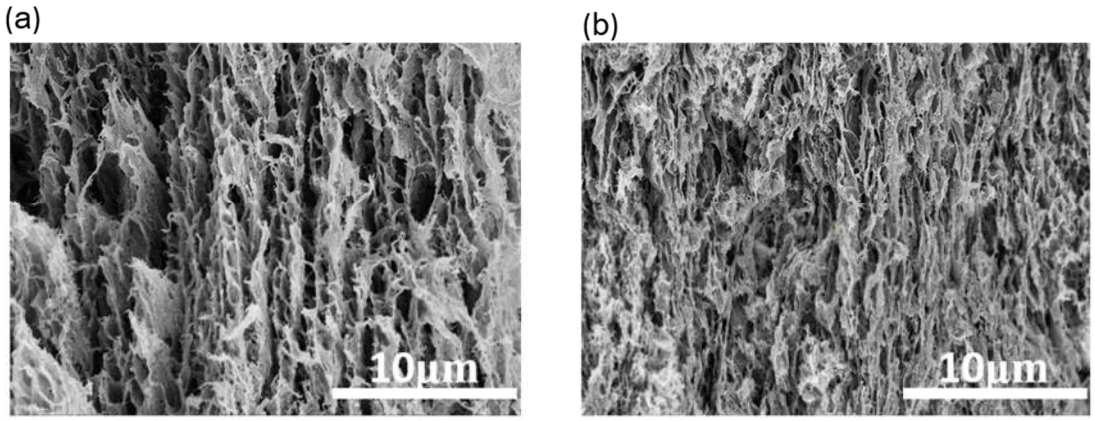

Figure S13. Morphology comparison before and after compression annealing.

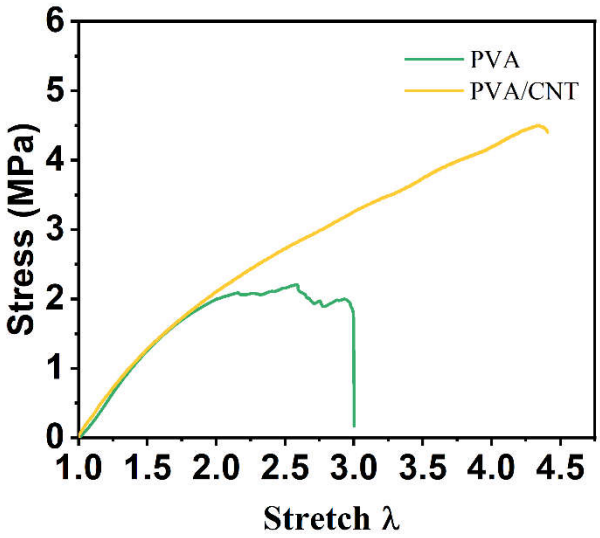

Figure S14. The stress-strain curve of PVA hydrogel and CNT enhanced PVA hydrogel

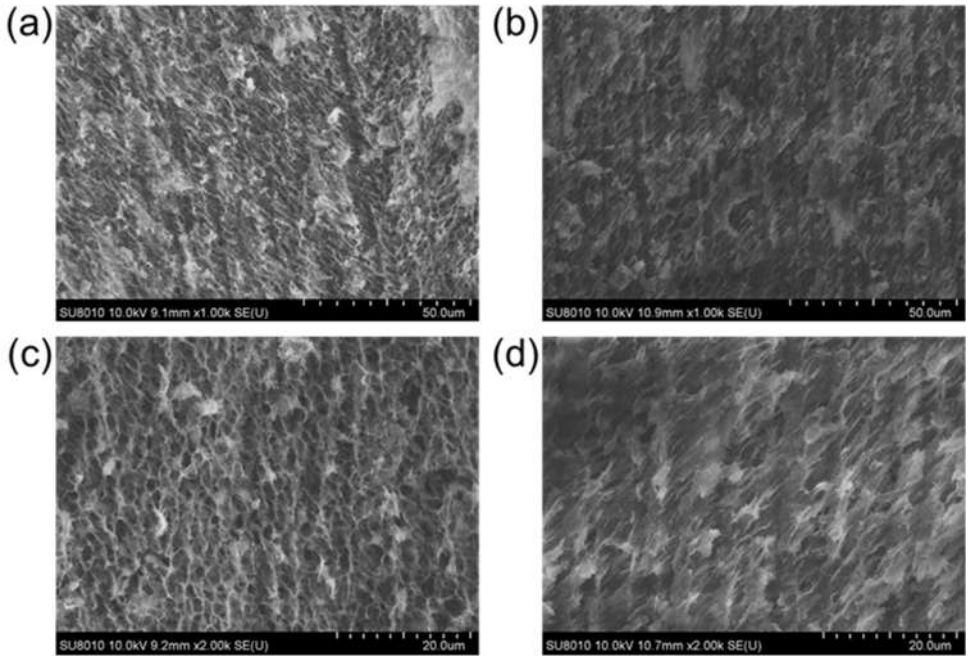

Figure S15. SEM of the salting out of PVA/CNT hydrogel, (a) and (c) are salting out samples, and (b) and (d) are samples without salting out.

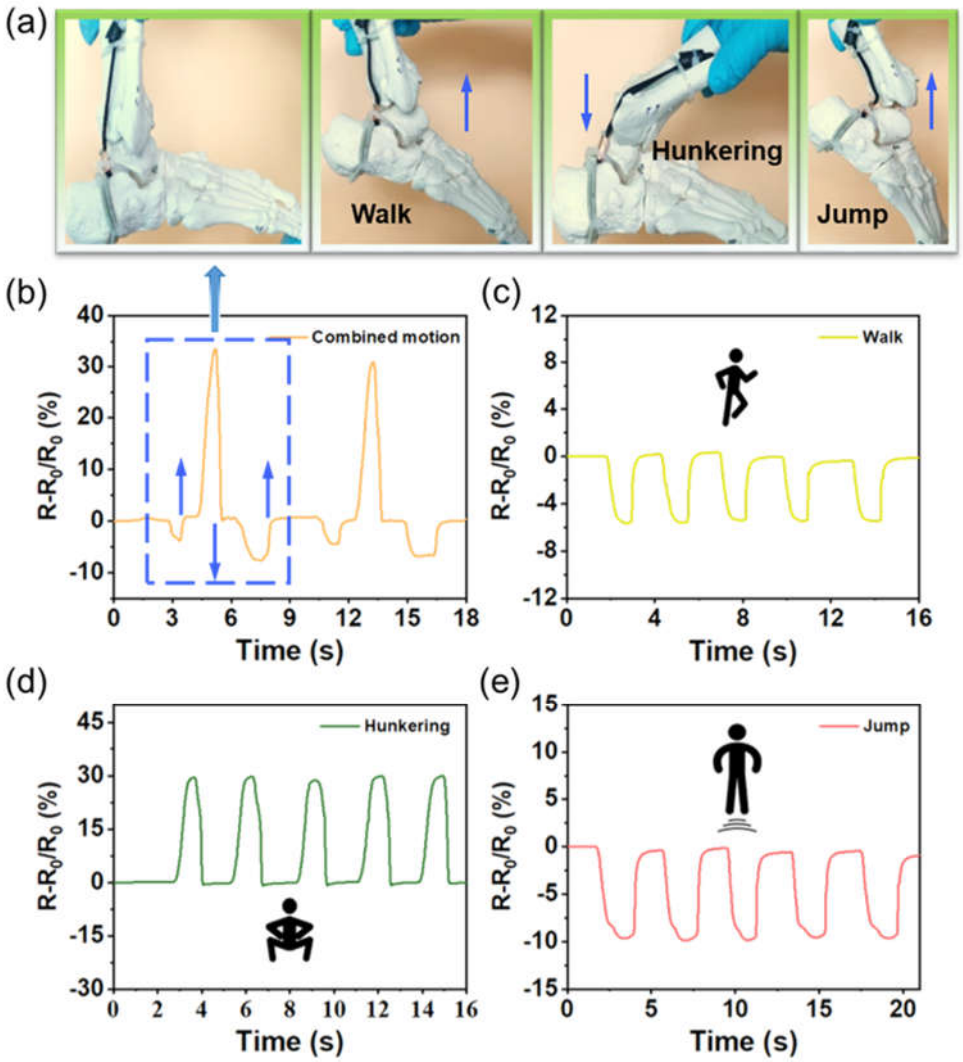

Figure S16. Simulation and monitoring of ligament motion. (a)The resistance of combined motion, (b) The resistance change of combined motion, (c)~(e) The resistance of individual motions

Figure S16a simulates a series of complex movements such as standing, walking, hunkering, and jumping. Figure S16b shows its corresponding continuous resistance change response. Sequential repetitions of individual actions are made in Figure S16c~ S16e. The ligaments are slightly bent in walking and stretched in squatting. When the leg jumps, it bends again. The corresponding signal has obvious and stable characteristic waveform, so the working state of artificial ligament can be monitored.

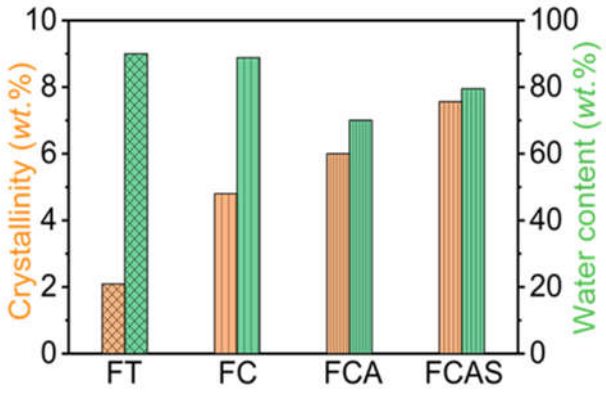

Figure S17. Crystallinity of FT, FC, FCA and FCAS

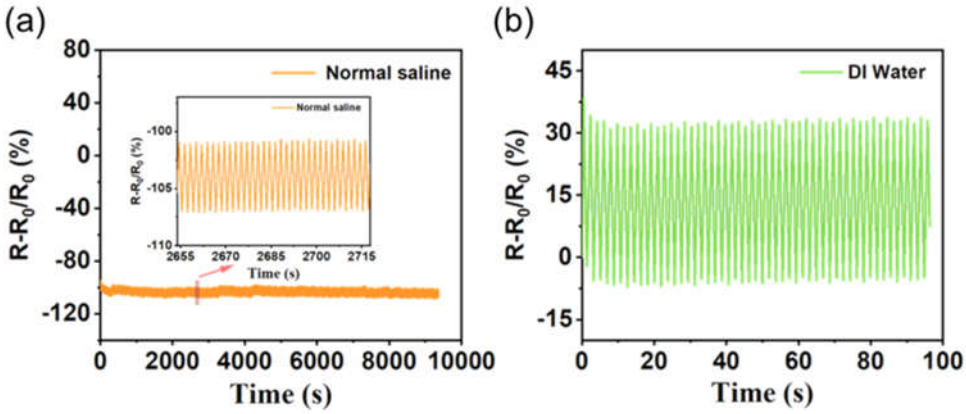

Figure S18. Circulatory stability in the body fluid environment

Table S1. Summary of the stretchable hydrogels using PVA in literature.

Tensile strength (MPa)	**Biocompatibility Test**	**water content (%)**	**Refs.**
0.75	Have	80	[1]
0.45	None	50-62.5	[2]
0.37	None	56	[3]
2.86	None	82.5-84	[4]
0.9	Have	84	[5]
1.7	None	58	[6]
1.1	None	24	[7]
0.25	None	30.2	[8]
0.53	None	47	[9]
4.5	Have	79.5	Our works

Reference

1. Z. Hu, J. Cheng, S. Xu, X. Cheng, J. Zhao, Z. W. Kenny Low, P. L. Chee, Z. Lu, L. Zheng and D. Kai, *Materials Today Bio*, 2022, DOI: 10.1016/j.mtbio.2022.100431.
2. Z. Zhou, Z. He, S. Yin, X. Xie and W. Yuan, *Composites Part B: Engineering*, 2021, **220**.
3. Y. Liu, W. Wang, K. Gu, J. Yao, Z. Shao and X. Chen, *ACS Appl Mater Interfaces*, 2021, **13**, 29008-29020.
4. X. Wang, X. Wang, M. Pi and R. Ran, *Chemical Engineering Journal*, 2022, **428**.
5. D. Liu, J. Qiu, R. Xu, J. Liu, J. Feng, L. Ouyang, S. Qian, Y. Qiao and X. Liu, *Composites Part B: Engineering*, 2022, **238**.
6. J. Yang, J. An, Y. Sun, J. Zhang, L. Zu, H. Li, T. Jiang, B. Chen and Z. L. Wang, *Nano Energy*, 2022, **97**.
7. Y. Nie, D. Yue, W. Xiao, W. Wang, H. Chen, L. Bai, L. Yang, H. Yang and D. Wei, *Chemical Engineering Journal*, 2022, **436**.
8. K. Hu, Z. Zhao, Y. Wang, L. Yu, K. Liu, H. Wu, L. Huang, L. Chen and Y. Ni, *Journal of Materials Chemistry A*, 2022, **10**, 12092-12103.
9. J. Lu, J. Gu, O. Hu, Y. Fu, D. Ye, X. Zhang, Y. Zheng, L. Hou, H. Liu and X. Jiang, *Journal of Materials Chemistry A*, 2021, **9**, 18406-18420.
10. X. Liang, G. Chen, S. Lin, J. Zhang, L. Wang, P. Zhang, Z. Wang, Z. Wang, Y. Lan, Q. Ge and J. Liu, *Adv Mater*, 2021, **33**, e2102011.
11. J. Liu, S. Lin, X. Liu, Z. Qin, Y. Yang, J. Zang and X. Zhao, *Nat Commun*, 2020, **11**, 1071.
12. R. Bai, J. Yang and Z. Suo, *European Journal of Mechanics-A/Solids*, 2019, 74,337-370.
13. S. Kotha, D. Ozturk, S. Ghosh. *International Journal of Plasticity*, 2019, 120,296-319.